Comput Mech (2009) 43:403–413
DOI 10.1007/s00466-008-0313-z

ORIGINAL PAPER

A linearly conforming radial point interpolation method (LC-RPIM) for shells

X. Zhao · G. R. Liu · K. Y. Dai · Z. H. Zhong · G. Y. Li · X. Han

Received: 26 October 2007 / Accepted: 16 June 2008 / Published online: 4 July 2008

Abstract In this paper, a linearly conforming radial point interpolation method (LC-RPIM) is presented for the linear analysis of shells. The first order shear deformation shell theory is adopted, and the radial and polynomial basis functions are employed to construct the shape functions. A strain smoothing stabilization technique for nodal integration is used to restore the conformability and to improve the accuracy. Convergence studies are performed in terms of the number of nodes and the nodal distribution patterns, including the regular distribution and the irregular distribution. Comparisons are made with the existing results available in the literature and good agreements are obtained. The numerical examples have demonstrated that the present approach provides very stable and accurate results and effectively eliminates the membrane locking and shear locking in shell problems.

Keywords Shell · Nodal integration · Radial basis function · Mesh-free · Shear locking

X. Zhao (✉) · G. R. Liu · K. Y. Dai
Department of Mechanical Engineering, Centre for Advanced Computations in Engineering Science (ACES),
The National University of Singapore, 9 Engineering Drive 1, Singapore 117576, Singapore
e-mail: alex.zx69@gmail.com

G. R. Liu
The Singapore-MIT Alliance (SMA), E4-04-10, 4 Engineering Drive 3, Singapore 117576, Singapore

Z. H. Zhong · G. Y. Li · X. Han
Key Laboratory of Advanced Technology for Vehicle Body Design and Manufacture, M.O.E, Hunan University, Changsha 410082, People's Republic of China

1 Introduction

The applications of shell structures are found in a variety of engineering fields, such as the aircraft and aerospace industry, marine industry and automobile industry. Hence, the shell analysis plays an important role in practical engineering circumstances. The commonly used methods for shell structures, to name a few, include the Ritz method, Finite element methods, and recently developed mesh-free methods. Numerous publications for the shell analysis using finite element methods have been reported since the forms of curved shell were proposed in the time of mid-1960 s. A lot of shell elements have been developed and their performances have been examined by researchers. Hughes and Liu [1,2] presented a nonlinear shell formulation based on the degenerated shell element, and Belytschko et al. [3] studied the performances of different quadrature schemes in dealing with membrane and shear locking in shells, and proposed a stress projection method to eliminate the membrane and shear locking in shell elements. Liu et al. [4] developed an efficient and reliable resultant-stress degenerated-shell element, which can avoid the problems of shear and membrane locking and spurious mode. Other notable works encompass those given by Simo et al. [5], Crisfield [6] and Reddy and Liu [7].

Meshfree methods, which are independent of the geometric elements, are considered as alternative methods for problems that are difficult to solve using conventional mesh-based approaches, and have been widely applied in various engineering analysis. Krysl and Belytschko [8] presented an element-free Galerkin shell formulation for arbitrary Kirchhoff shells. Noguchi et al. [9] proposed an enhanced element-free Galerkin method to analyze three-dimensional shell and spatial structures. Li et al. [10] carried out the numerical simulations of large deformation of thin shell structures using the meshfree reproducing kernel particle method. Liu et al. [11] developed a new class of methods, the reproducing kernel element method (RKEM), which utilizes the advantages of both finite element methods and meshfree methods. The interpolation hierarchical structure was constructed with both minimal degrees of freedom and higher order smoothness continuity over multi-dimensional domain [12,13].

In meshfree methods, numerical integration is commonly carried out on the background elements using the Gaussian quadrature. In order to reduce the computation cost and avoid the complexity involved in the Gauss integration in meshfree methods, the nodal integration has been proposed by researchers as an alternative of the Gaussian quadrature. Beissel and Belytschko [14] presented a stabilized nodal integration approach in element-free Galerkin method. Their study demonstrated that the stabilized EFG eliminated spurious near-singular modes in some problems. For problems without unstable modes, however, the accuracy of solutions deteriorated. Bonet and Kulasegaram [15] provided a correction procedure to improve the accuracy of nodal integration by avoiding the computation of a second-order derivative of shape functions. Chen et al. [16] proposed a stabilized nodal integration procedure for the Galerkin meshfree method to achieve higher efficiency with desired accuracy and convergent properties. An integration constraint (IC) is introduced as a necessary condition for a linear exactness in the meshfree Galerkin approximation. They have demonstrated that the Gauss integration methods violate IC and produce prominent errors. Using the stabilized conforming nodal integration, Wang and Chen [17] presented a meshfree Mindlin–Reissner plate formulation to mitigate the shear locking in Mindlin–Reissner plates.

The Point Interpolation Method (PIM), a meshfree method based on Galerkin formulation, was originally proposed by Liu and Gu [18] and used for solid mechanics problems. Later, Wang and Liu [19] presented an alternative version of PIM, the radial point interpolation method (RPIM), where both polynomial and radial basis functions (RBFs) are employed to construct the shape functions in terms of a set of arbitrarily distributed nodes. The RPIM shape functions possess the Kronecker delta function properties, the boundary conditions, therefore, can be imposed directly. Moreover, due to the adoption of the radial basis function, the moment matrix is always convertible for arbitrarily scattered nodes. The RPIM has been successfully applied in various engineering problems, such as simulation of piezoelectric structures [20], three-dimensional elasticity problems [21], and solid mechanics problems [22].

In this paper, a linearly conforming radial point interpolation method (LC-RPIM) is presented for the linear analysis of shell structures. A stabilized nodal integration technique is used to achieve conformity, higher accuracy and efficiency. The first order shear deformation shell theory is employed in this formulation. The numerical examples demonstrate that the present method shows the good accuracy, efficiency and stability, and is effective in eliminating the membrane and shear locking in shell problems.

2 Radial point interpolation method (RPIM)

In this section, the construction of shape functions based on RPIM is briefly introduced. Consider a domain with a set of arbitrarily scattered points at $\mathbf{x}_i$, $(i = 1, 2, \ldots, n)$, where n is the number of nodes in the support domain. The approximation of a continuous function $u(\mathbf{x})$ can be expressed in the form of

$$u(\mathbf{x}) = \sum_{i=1}^{n} r_i(\mathbf{x})a_i + \sum_{j=1}^{m} p_j(\mathbf{x})b_j = \mathrm{r}^{\mathrm{T}}(\mathbf{x})\mathbf{a} + \mathbf{P}^{\mathrm{T}}(\mathbf{x})\mathbf{b} \tag{1}$$

where a_i is the unknown coefficient for the radial basis function $r_i(\mathbf{x})$, which is defined as

$$r_i(x, y) = \left[(x - x_i)^2 + (y - y_i)^2 + R_c^2\right]^q \tag{2}$$

where q and R_c are shape parameters, which are arbitrary real numbers and had been examined in detail by Wang and Liu [19]. In Eq. (1), b_j is the coefficient for the polynomial basis $p_j(\mathbf{x})$, and m is determined according to the polynomial basis selected. For example, a quadratic basis in two-dimension requires $m = 6$, and the polynomial base are given by

$$\mathbf{P}^{\mathrm{T}}(\mathbf{x}) = \left[1, x, y, x^2, xy, y^2\right] \tag{3}$$

The coefficients a_i and b_j are determined by satisfying the reproducing condition at the nodes in the support domain. The interpolation at the kth node is expressed as

$$u_k = u(\mathbf{x}_k) = \sum_{i=1}^{n} a_i r_i(\mathbf{x}_k) + \sum_{j=1}^{m} b_j p_j(\mathbf{x}_k), \quad k = 1,\ 2, \ldots,\ n \tag{4}$$

In order to solve coefficients a_i and b_j uniquely, the following constraints are imposed

$$\sum_{i=1}^{n} p_j(\mathbf{x}_k)a_i = 0, \quad j = 1, 2, \ldots, m \tag{5}$$

It can be expressed in matrix form as

$$\begin{bmatrix} \mathbf{R}_0 & \mathbf{P}_0 \\ \mathbf{P}_0^{\mathrm{T}} & \mathbf{0} \end{bmatrix} \begin{Bmatrix} \mathbf{a} \\ \mathbf{b} \end{Bmatrix} = \begin{Bmatrix} \mathbf{u}^e \\ \mathbf{0} \end{Bmatrix} \quad \text{or} \quad \mathbf{G} \begin{Bmatrix} \mathbf{a} \\ \mathbf{b} \end{Bmatrix} = \begin{Bmatrix} \mathbf{u}^e \\ \mathbf{0} \end{Bmatrix} \tag{6}$$

where nodal displacement vector $\mathbf{u}^e$ is given by

$$\mathbf{u}^e = [u_1, u_2, u_3, \ldots, u_n]^{\mathrm{T}} \tag{7}$$

The moment matrix $\mathbf{R}_0$ is expressed as

$$\mathbf{R}_0 = \begin{bmatrix} r_1(x_1, y_1) & r_2(x_1, y_1) & \cdots & r_n(x_1, y_1) \\ r_1(x_2, y_2) & r_2(x_2, y_2) & \cdots & r_n(x_2, y_2) \\ \vdots & \vdots & \vdots & \vdots \\ r_1(x_n, y_n) & r_2(x_n, y_n) & \cdots & r_n(x_n, y_n) \end{bmatrix} \quad (8)$$

and the matrix $\mathbf{P}_0$ is defined as

$$\mathbf{P}_0 = \begin{bmatrix} p_1(x_1, y_1) & p_2(x_1, y_1) & \cdots & p_m(x_1, y_1) \\ p_1(x_2, y_2) & p_2(x_2, y_2) & \cdots & p_m(x_2, y_2) \\ \vdots & \vdots & \vdots & \vdots \\ p_1(x_n, y_n) & p_2(x_n, y_n) & \cdots & p_m(x_n, y_n) \end{bmatrix} \quad (9)$$

Solving Eq. (6) yields

$$\begin{Bmatrix} \mathbf{a} \\ \mathbf{b} \end{Bmatrix} = \mathbf{G}^{-1} \begin{Bmatrix} \mathbf{u}^e \\ \mathbf{0} \end{Bmatrix} \quad (10)$$

The approximation of the function $u(\mathbf{x})$ is finally expressed as

$$\mathbf{u}(\mathbf{x}) = \left[\mathbf{R}_0^{\mathrm{T}}(\mathbf{x})\ \mathbf{P}_0^T(\mathbf{x}) \right] \mathbf{G}^{-1} \begin{Bmatrix} \mathbf{u}^e \\ \mathbf{0} \end{Bmatrix} = \boldsymbol{\varphi}(\mathbf{x})\mathbf{u}^e \quad (11)$$

where $\boldsymbol{\varphi}(\mathbf{x})$ is the matrix of the shape functions and given by

$$\boldsymbol{\varphi}(\mathbf{x}) = [\phi_1(\mathbf{x})\, \phi_2(\mathbf{x}) \cdots \phi_n(\mathbf{x})]$$
$$\phi_k(\mathbf{x}) = \sum_{i=1}^{n} r_i(\mathbf{x})\bar{G}_{i,k} + \sum_{j=1}^{m} p_j(\mathbf{x})\bar{G}_{n+j,k} \quad (12)$$

where $\bar{G}_{i,k}$ is the element of the matrix $\mathbf{G}^{-1}$. Thus, an approximation function $u^h(\mathbf{x})$ can be expressed as

$$u^h(\mathbf{x}) = \sum_{I=1}^{NP} \phi_I(\mathbf{x})\mathbf{u}_I^e \quad (13)$$

The derivatives of shape functions can be obtained by differentiating Eq. (12)

$$\frac{\partial \phi_k}{\partial x} = \sum_{i=1}^{n} \frac{\partial r_i}{\partial x}\bar{G}_{i,k} + \sum_{j=1}^{m} \frac{\partial p_j}{\partial x}\bar{G}_{n+j,k}$$
$$\frac{\partial \phi_k}{\partial y} = \sum_{i=1}^{n} \frac{\partial r_i}{\partial y}\bar{G}_{i,k} + \sum_{j=1}^{m} \frac{\partial p_j}{\partial y}\bar{G}_{n+j,k} \quad (14)$$

The present shape functions possess the reproducing properties due to the addition of polynomial basis, satisfy the Delta function properties and partition of unity, and always exist because of the adoption of RBFs.

3 Strain smoothing technique

3.1 Integration constraints

Chen et al. [16] have demonstrated that, for linear exactness in Galerkin approximation, integration constraints (IC) need to be satisfied in domain integration. The integration constraints are given by

$$\sum_{L=1}^{\mathrm{NIT}} \nabla\phi_I(\hat{\mathbf{x}}_L)w_L = 0 \text{ for all interior nodes}$$
$$\{I : \mathrm{supp}(\phi_I) \cap \Gamma = \emptyset\} \quad (15)$$
$$\sum_{L=1}^{\mathrm{NIT}} \nabla\phi_I(\hat{\mathbf{x}}_L)w_L = \sum_{L=1}^{\mathrm{NITh}} \mathbf{n}\phi_I(\hat{\mathbf{x}}_L)s_L \text{ for boundary nodes}$$
$$\{I : \mathrm{supp}\,(\phi_I) \cap \Gamma^h \neq \emptyset\} \quad (16)$$

where Γ is the entire boundary; Γ^h is the natural boundary; $\mathbf{n}$ is the surface normal on Γ^h; $\hat{\mathbf{x}}_L$ and w_L are the spatial co-ordinate and the weight of the domain integration point, respectively; $\hat{\mathbf{x}}_L$ and s_L in Eq. (16) are spatial co-ordinate and weight of natural boundary integration point; NIT is the number of domain integration points, and NITh is the number of integration points on the natural boundary.

3.2 Strain smoothing technique

The strain smoothing approach that meets integration constraint was proposed by Chen [16] to remove the instability in the nodal integration. For a representative domain of a node $\mathbf{x}_L$, the strain smoothing at the node is given by

$$\tilde{\varepsilon}_{ij}(\mathbf{x}_L) = \int_{\Omega} \varepsilon_{ij}(\mathbf{x})\Phi(\mathbf{x}; \mathbf{x} - \mathbf{x}_L)d\Omega \quad (17)$$

where ε_{ij} is the strain obtained from displacement, and Φ is a smoothing function. A constant smoothing function is written as

$$\Phi(\mathbf{x}; \mathbf{x} - \mathbf{x}_L) = \begin{cases} 1/A_L & \mathbf{x} \in \Omega_L \\ 0 & \mathbf{x} \notin \Omega_L \end{cases} \quad (18)$$

in which $A_L = \int_{\Omega_L} d\Omega$ is the area of the representative domain of node L, which can be obtained either from the Voronoi diagram or Delaunay triangulation shown in Fig. 1. Employing the divergence theorem to Eq. (17) yields the following strain smoothing expression

$$\tilde{\varepsilon}_{ij}(\mathbf{x}_L) = \frac{1}{2A_L} \int_{\Gamma_L} \mathbf{n}u_i^h d\Gamma \quad (19)$$

where Γ_L is the boundary of the representative domain of node L, and $\mathbf{n}$ is the surface normal on Γ_L, as shown in Fig. 2. For a two-dimensional problem, introducing RPIM

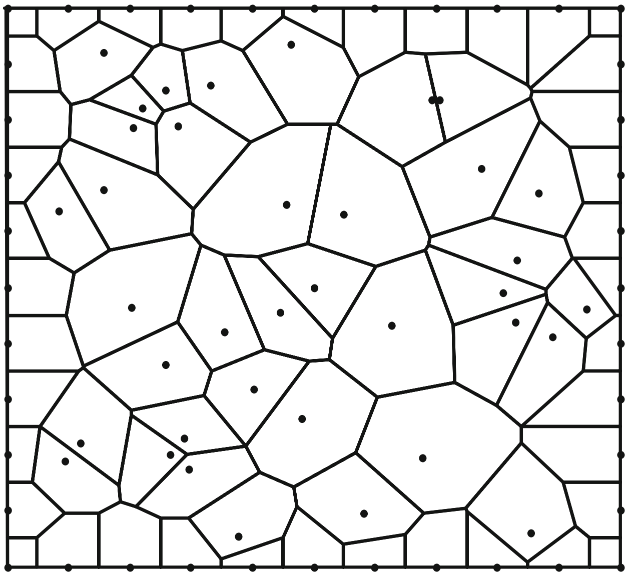

(a) Voronoi diagram

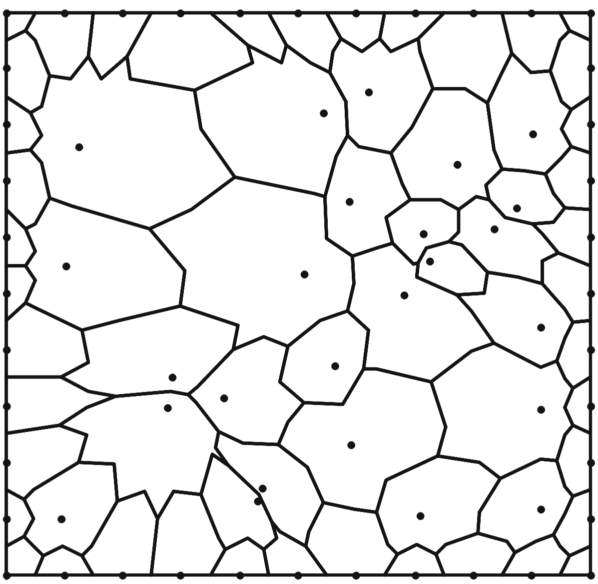

(b) Nodal domain by Delaunay triangulation

Fig. 1 Problem domain represented by irregular nodes: **a** Voronoi diagram; **b** nodal domain by Delaunay triangulation

shape functions into Eq. (19) yields

$$\tilde{\boldsymbol{\varepsilon}}^h(x_L) = \sum_{I \in S_L} \tilde{\mathbf{B}}_I(\mathbf{x}_L)\mathbf{u}_I \tag{20}$$

$$\tilde{\mathbf{B}}_I(\mathbf{x}_L) = \begin{bmatrix} \tilde{\nabla}_1\phi_I(\mathbf{x}_L) & 0 \\ 0 & \tilde{\nabla}_2\phi_I(\mathbf{x}_L) \\ \tilde{\nabla}_2\phi_I(\mathbf{x}_L) & \tilde{\nabla}_1\phi I(\mathbf{x}_L) \end{bmatrix} \tag{21}$$

$$\tilde{\nabla}_i\phi_I(\mathbf{x}_L) = \frac{1}{A_L}\int_{\Gamma_L} \phi_I(\mathbf{x}_L)n_i(\mathbf{x}_L)d\Gamma \quad (i = 1,\ 2) \tag{22}$$

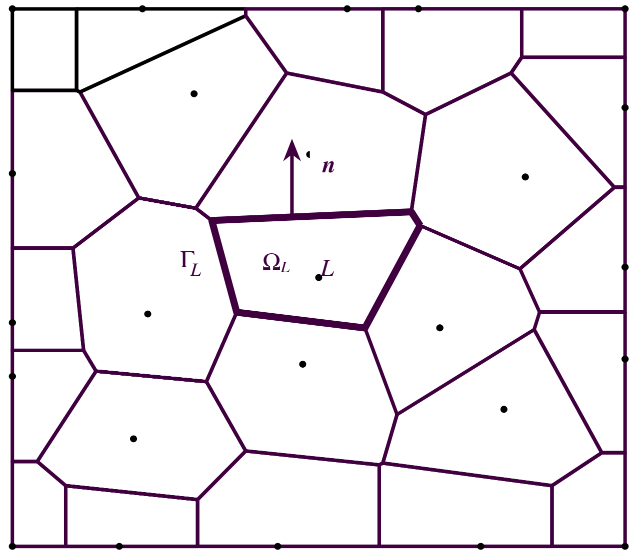

Fig. 2 A nodal representative domain

where S_L is a group of nodes in the corresponding support for node L. It has been demonstrated that the smoothing gradient Eq. (22) satisfies the integration constraints in Eqs. (15) and (16) when the reproducing kernel shape functions are introduced [16]. Due to the reproducing properties of the RPIM shape functions, it is obviously seen that the integration constraints in Eqs. (15) and (16) still hold when the RPIM shape functions are employed.

4 Formulation

4.1 Energy formulation

Figure 3a shows a doubly-curved shell panel, an orthogonal curvilinear coordinate system (x, y, z) is fixed on the middle surface of the panel. The parameters R_1 and R_2 denote the principal radii of curvature of the middle surface, h represents the thickness. The cylindrical shell panel shown in Fig. 3b is a special case of a doubly curved shell panel when $R_1 = \infty$ and $R_2 = R$. For a shell panel with $R_1 = R_2 = R$, it becomes a spherical shell. In present study, both the circular cylindrical shells and the spherical shells are considered.

According to the first order shear deformation shell theory [23], the displacement field is expressed as

$$\begin{aligned} u(x, y, z) &= u_0(x, y) + z\psi_x(x, y) \\ v(x, y, z) &= v_0(x, y) + z\psi_y(x, y) \\ w(x, y, z) &= w_0(x, y) \end{aligned} \tag{23}$$

where u_0, v_0 and w_0 denote the displacements of the middle surface of the shell in the x, y, and z directions, ψ_x and ψ_y are the rotations of the transverse normal about the y and x axes, respectively.

The linear strains are defined as

$$\begin{Bmatrix} \varepsilon_{xx} \\ \varepsilon_{yy} \\ \gamma_{xy} \end{Bmatrix} = \boldsymbol{\varepsilon}_0 + z\boldsymbol{\kappa}, \quad \begin{Bmatrix} \gamma_{yz} \\ \gamma_{xz} \end{Bmatrix} = \boldsymbol{\gamma}_0 \tag{24}$$

where

$$\boldsymbol{\varepsilon}_0 = \begin{Bmatrix} \dfrac{\partial u_0}{\partial x} + \dfrac{w_0}{R_1} \\ \dfrac{\partial v_0}{\partial y} + \dfrac{w_0}{R_2} \\ \dfrac{\partial u_0}{\partial y} + \dfrac{\partial v_0}{\partial x} \end{Bmatrix}, \quad \boldsymbol{\kappa} = \begin{Bmatrix} \dfrac{\partial \psi_x}{\partial x} \\ \dfrac{\partial \psi_y}{\partial y} \\ \dfrac{\partial \psi_x}{\partial y} + \dfrac{\partial \psi_y}{\partial x} \end{Bmatrix},$$

$$\boldsymbol{\gamma}_0 = \begin{Bmatrix} \psi_y + \dfrac{\partial w_0}{\partial y} \\ \psi_x + \dfrac{\partial w_0}{\partial x} \end{Bmatrix} \tag{25}$$

The total strain energy of the panel is expressed by

$$U_\varepsilon = \frac{1}{2} \int\limits_\Omega \boldsymbol{\varepsilon}^{\mathrm{T}} \mathrm{S} \boldsymbol{\varepsilon} d\Omega \tag{26}$$

where $\boldsymbol{\varepsilon}$ and $\mathbf{S}$ are given by

$$\boldsymbol{\varepsilon} = \left\{ \boldsymbol{\varepsilon}_0 \ \boldsymbol{\kappa} \ \boldsymbol{\gamma}_0 \right\}^{\mathrm{T}} \tag{27}$$

$$\mathbf{S} = \begin{bmatrix} A_{11} & A_{12} & A_{16} & B_{11} & B_{12} & B_{16} & 0 & 0 \\ A_{12} & A_{22} & A_{26} & B_{12} & B_{22} & B_{26} & 0 & 0 \\ A_{16} & A_{26} & A_{66} & B_{16} & B_{26} & B_{66} & 0 & 0 \\ B_{11} & B_{12} & B_{16} & D_{11} & D_{12} & D_{16} & 0 & 0 \\ B_{12} & B_{22} & B_{26} & D_{12} & D_{22} & D_{26} & 0 & 0 \\ B_{16} & B_{26} & B_{66} & D_{16} & D_{26} & D_{66} & 0 & 0 \\ 0 & 0 & 0 & 0 & 0 & 0 & S_{44} & S_{45} \\ 0 & 0 & 0 & 0 & 0 & 0 & S_{45} & S_{55} \end{bmatrix}$$

$$= \begin{bmatrix} \mathbf{A} & \widehat{\mathbf{B}} & \mathbf{0} \\ \widehat{\mathbf{B}} & \mathbf{D} & \mathbf{0} \\ \mathbf{0} & \mathbf{0} & \bar{\mathbf{S}} \end{bmatrix} = \begin{bmatrix} \bar{\mathbf{D}} & \mathbf{0} \\ \mathbf{0} & \bar{\mathbf{S}} \end{bmatrix} \tag{28}$$

In which the extensional A_{ij}, coupling B_{ij}, bending D_{ij} and transverse shear S_{ij} stiffnesses, are given by

$$(A_{ij}, B_{ij}, D_{ij}) = \int\limits_{-h/2}^{h/2} Q_{ij}(1, z, z^2) dz, \quad S_{ij} = \int\limits_{-h/2}^{h/2} K Q_{ij} dz \tag{29}$$

The stiffness A_{ij}, B_{ij}, and D_{ij} are defined for $i, j = 1, 2, 6$, whereas S_{ij} is defined for $i, j = 4, 5$. K denotes the transverse shear correction coefficient and is taken as $K = 5/6$. Q_{ij} is the engineering constant and is defined as

$$Q_{11} = \frac{E_{11}}{1 - \nu_{12}\nu_{21}}, \quad Q_{12} = \frac{\nu_{12} E_{22}}{1 - \nu_{12}\nu_{21}}, \quad Q_{22} = \frac{E_{22}}{1 - \nu_{12}\nu_{21}}$$
$$Q_{66} = G_{12}, \quad Q_{44} = G_{23}, \quad Q_{55} = G_{13}, \tag{30}$$

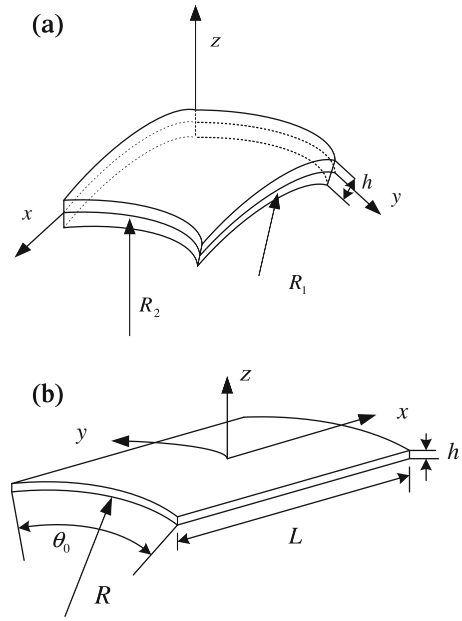

Fig. 3 **a** Geometry of a doubly-curved shell panel. **b** Geometry of a cylindrical shell panel

where E_{11} and E_{22} are the elastic moduli in the principle material coordinates, G_{12}, G_{13}, and G_{23} are the shear moduli, and ν_{12} and ν_{21} are the Poisson's ratios. For a shell composed of different layers of materials, the stiffnesses in Eq. (29) can be computed according to the method introduced by Reddy and Miravete [24]

The external work done due to the surface traction and body force is expressed as

$$W_e = \int\limits_\Omega \mathbf{u}^{\mathrm{T}} \bar{\mathbf{f}} d\Omega + \int\limits_\Gamma \mathbf{u}^{\mathrm{T}} \bar{\mathbf{t}} d\Gamma \tag{31}$$

where $\bar{\mathbf{f}}$ and $\bar{\mathbf{t}}$ represent the external load and the prescribed traction on the natural boundary, respectively.
Thus, the total potential energy functional of the panel is written as

$$\Pi_s = U_\varepsilon - W_e \tag{32}$$

4.2 Nodal integration

In order to perform the nodal integration, a set of discrete nodes is freely generated on the $x - y$ space in the parametric coordinate system. The corresponding nodal representative domains are formed according to the Delaunay triangulation. For a shell panel domain Ω discretized by a set of nodes x_I, $I = 1, \ldots, NP$, the approximations of the displacements and rotations of the mid-surface of the panel are expressed as

$$\mathbf{u}_0^h = \begin{pmatrix} u_0^h \\ v_0^h \\ w_0^h \\ \theta_x^h \\ \theta_y^h \end{pmatrix} = \sum_{I=1}^{NP} \phi_I \begin{pmatrix} u_I \\ v_I \\ w_I \\ \theta_{xI} \\ \theta_{yI} \end{pmatrix} = \sum_{I=1}^{NP} \phi_I(\mathbf{x})\mathbf{d}_I \tag{33}$$

Substituting Eq. (33) into Eq. (32) and taking variation to the energy functional yields the equation

$$\mathbf{Kd} = \mathbf{f} \tag{34}$$

where

$$\mathbf{K} = \mathbf{K}^b + \mathbf{K}^m + \mathbf{K}^s \tag{35}$$

$$\mathbf{d} = [\mathbf{d}_1\, \mathbf{d}_2\, \cdots\, \mathbf{d}_n]^{\mathrm{T}} \tag{36}$$

$$\mathbf{K}_{IJ}^b = \int_\Omega \mathbf{B}_I^{b\,\mathrm{T}} \mathbf{D} \mathbf{B}_J^b d\Omega \tag{37}$$

$$\mathbf{K}_{IJ}^m = \int_\Omega \mathbf{B}_I^{m\,\mathrm{T}} \mathbf{A} \mathbf{B}_J^m d\Omega + \int_\Omega \mathbf{B}_I^{m\,\mathrm{T}} \widehat{\mathbf{B}} \overset{b}{\mathbf{B}}_J d\Omega + \int_\Omega \mathbf{B}_I^{b\,\mathrm{T}} \widehat{\mathbf{B}} \overset{m}{\mathbf{B}}_J d\Omega \tag{38}$$

$$\mathbf{K}_{IJ}^s = \int_\Omega \mathbf{B}_I^{s\,\mathrm{T}} \bar{\mathbf{S}} \mathbf{B}_J^s d\Omega \tag{39}$$

$$\mathbf{f}_I = \int_\Omega \phi_I \bar{\mathbf{f}} d\Omega + \int_\Gamma \phi_I \bar{\mathbf{t}} d\Gamma \tag{40}$$

The stiffness matrix in Eq. (37) is evaluated by using the stabilized nodal integration technique introduced in Sect. 3, whereas Eqs. (38)–(40) are computed by using the direct nodal integration. The approximations of Eqs. (37)–(40) are given as

$$\mathbf{K}_{IJ}^b = \sum_{L=1}^{NP} \tilde{\mathbf{B}}_I^{b\,\mathrm{T}}(\mathbf{x}_L) \mathbf{D} \tilde{\mathbf{B}}_J^b(\mathbf{x}_L) A_L \tag{41}$$

$$\mathbf{K}_{IJ}^m = \sum_{L=1}^{NP} \left[\mathbf{B}_I^{m\,T}(\mathbf{x}_L) \mathbf{A} \mathbf{B}_J^m(\mathbf{x}_L) + \mathbf{B}_I^{m\,\mathrm{T}}(\mathbf{x}_L) \widehat{\mathbf{B}} \overset{b}{\mathbf{B}}_J(\mathbf{x}_L) + \mathbf{B}_I^{b\,\mathrm{T}}(\mathbf{x}_L) \widehat{\mathbf{B}} \overset{m}{\mathbf{B}}_J(\mathbf{x}_L) \right] A_L \tag{42}$$

$$\mathbf{K}_{IJ}^s = \sum_{L=1}^{NP} \mathbf{B}_I^{s\,\mathrm{T}}(\mathbf{x}_L) \bar{\mathbf{S}} \mathbf{B}_J^s(\mathbf{x}_L) A_L \tag{43}$$

$$\mathbf{f}_I = \sum_{L=1}^{NP} \phi_I(\mathbf{x}_L) \mathbf{f}(\mathbf{x}_L) A_L + \sum_{L=1}^{NPb} \phi_I(\mathbf{x}_L) \bar{\mathbf{t}}(\mathbf{x}_L) s_L \tag{44}$$

where $\mathbf{x}_L$ and A_L denote the nodal point coordinate and the nodal representative area, respectively, NPb is the number of nodes on the natural boundary, and s_L are the weights associated with the boundary point obtained from Delaunay triangulation. $\tilde{\mathbf{B}}_I^b(\mathbf{x}_L)$, $\mathbf{B}_I^b(\mathbf{x}_L)$, $\mathbf{B}_I^m(\mathbf{x}_L)$ and $\mathbf{B}_I^s(\mathbf{x}_L)$ are given by

$$\tilde{\mathbf{B}}_I^b(\mathbf{x}_L) = \begin{bmatrix} 0 & 0 & 0 & \tilde{b}_{Ix}(\mathbf{x}_L) & 0 \\ 0 & 0 & 0 & 0 & \tilde{b}_{Iy}(\mathbf{x}_L) \\ 0 & 0 & 0 & \tilde{b}_{Iy}(\mathbf{x}_L) & \tilde{b}_{Ix}(\mathbf{x}_L) \end{bmatrix} \tag{45}$$

$$\tilde{b}_{Ix}(\mathbf{x}_L) = \frac{1}{A_L} \int_{\Gamma_L} \phi_I(\mathbf{x}) n_x(\mathbf{x}) d\Gamma \tag{46}$$

$$\tilde{b}_{Iy}(\mathbf{x}_L) = \frac{1}{A_L} \int_{\Gamma_L} \phi_I(\mathbf{x}) n_y(\mathbf{x}) d\Gamma \tag{47}$$

$$\mathbf{B}_I^b(\mathbf{x}_L) = \begin{bmatrix} 0 & 0 & 0 & \frac{\partial \phi_I(\mathbf{x}_L)}{\partial x} & 0 \\ 0 & 0 & 0 & 0 & \frac{\partial \phi_I(\mathbf{x}_L)}{\partial y} \\ 0 & 0 & 0 & \frac{\partial \phi_I(\mathbf{x}_L)}{\partial y} & \frac{\partial \phi_I(\mathbf{x}_L)}{\partial x} \end{bmatrix} \tag{48}$$

$$\mathbf{B}_I^m(\mathbf{x}_L) = \begin{bmatrix} \frac{\partial \phi_I(\mathbf{x}_L)}{\partial x} & 0 & \frac{\phi_I(\mathbf{x}_L)}{R_1} & 0 & 0 \\ & \frac{\partial \phi_I(\mathbf{x}_L)}{\partial y} & \frac{\phi_I(\mathbf{x}_L)}{R_2} & 0 & 0 \\ \frac{\partial \phi_I(\mathbf{x}_L)}{\partial y} & \frac{\partial \phi_I(\mathbf{x}_L)}{\partial x} & 0 & 0 & 0 \end{bmatrix} \tag{49}$$

$$\mathbf{B}_I^s(\mathbf{x}_L) = \begin{bmatrix} 0 & 0 & \frac{\partial \phi_I(\mathbf{x}_L)}{\partial x} & \phi_I(\mathbf{x}_L) & 0 \\ 0 & 0 & \frac{\partial \phi_I(\mathbf{x}_L)}{\partial y} & 0 & \phi_I(\mathbf{x}_L) \end{bmatrix} \tag{50}$$

5 Numerical examples

In this section, several benchmark problems are presented to evaluate the performance of the present method. The shape functions are constructed using the radial point interpolation method, the shape parameters q and R_c are taken as 1.03 and 1.42, respectively [19]. A scaling factor of 3.4 for a support domain is selected. The nodal integration domain is generated by Delaunay triangulation. The trapezoidal rule with two-point on each segment for the integration is adopted. The smoothing stabilization technique is used in evaluating the bending stiffness, while the membrane and shear stiffness terms are estimated by using the direct nodal integration method for the elimination of the membrane locking and shear locking.

5.1 Scordelis-Lo roof

The Scordelis-Lo roof, or Barrel vault roof, is a famous benchmark problem for the shell analysis to test the membrane response. Figure 4 shows the barrel vault loaded by gravity forces. The boundary at the curved edges is rigid diaphragm and the two straight edges are free. The geometric properties of the shell are: the length $L = 600$ in, the radius $R = 300$ in, the thickness $h = 3$ in, and the span angle $\theta_0 = 0.6981$ rad or $\theta_0 = 80°$. The material properties are: $E = 3 \times 10^6$ psi and $\nu = 0.0$. The dead weight loading is $q_0 = 0.625$ psi. A quarter of the roof is modeled because of the symmetry. In this case, a value of 3.6288in is taken as the

Fig. 4 A cylindrical shell roof under its own weight

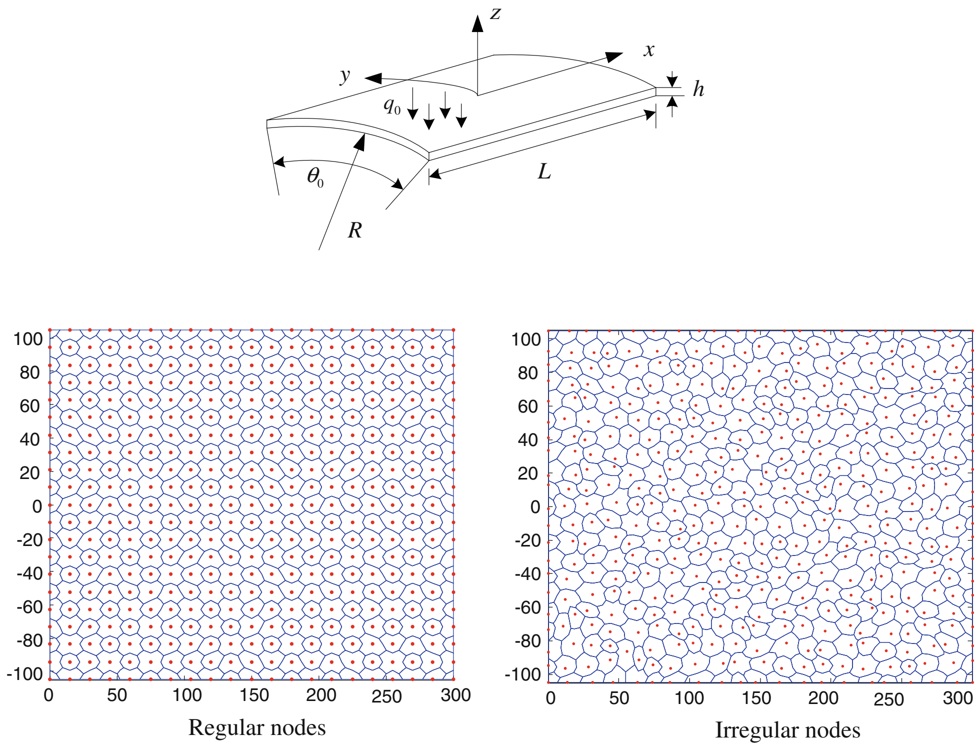

reference solution for the vertical deflection at the center of the free edge [5,23]. All solutions given in this case are normalized with the reference value. Two cases are studied for this problem: regularly distributed nodes and irregularly distributed nodes. Figure 5 shows the comparisons of the present results obtained from using a regular nodal distribution with solutions produced from FEM using 4-node and 9-node elements with reduced integration and other elements [4,25]. It is seen that the RPIM shows a very good convergence performance. The vertical displacement of the center line of the roof is plotted in Fig. 6. It is observed that the result derived from the proposed method agrees with the solution by FEM [23] very well. Table 1 shows the comparison between the present solution with those obtained from NUHEX-4 element and NUHEXIN-4 element [26], and HEXDS element [27]. It is seen that, for the regular nodal distribution, the NUHEX-4 element shows the best convergence performance, the RPIM, however, can achieve the same accuracy of the solution with 32×32 nodes. Compared with the NUHEXIN-4 and HEXDS element, the RPIM demonstrates a better convergence performance and produces more accurate result. To examine the effects of the nodal distribution pattern on the solution, the irregular nodal distribution is generated by manipulating the regular nodes according to the following approach:

$$
\begin{aligned}
x_{ir} &= x + \Delta x \cdot r_c \cdot \alpha_{ir} \\
y_{ir} &= y + \Delta y \cdot r_c \cdot \alpha_{ir}
\end{aligned} \tag{51}
$$

where x and y are the coordinates of regular nodes, Δx and Δy are initial nodal spacings, r_c is a random number between -1 and 1, α_{ir} represents the irregularity factor ranging from 0.1 to 0.4, a higher value of α_{ir} means that the nodes are more highly irregular. The result in Table 1 is obtained using an irregular factor of 0.4. It is seen that the influence of the irregularity seems more pronounced than that of the number of nodes.

Although the result produced from the irregularly distributed nodes is less accurate, the difference is limited in a range of 3–19%.

5.2 Pinched cylinder

This is a known benchmark for cylindrical shells, and is identified as one of the most severe tests for inextensional bending and complex membrane states. The pinched shell is supported at each end by rigid diaphragm and subjected to a pair of pinching loads $P = 1$, as shown in Fig. 7. The geometric properties of the cylinder are: length $L = 600$ in, radius $R = 300$ in, and thickness $h = 3$ in. The material constants are: Young's modulus $E = 3 \times 10^6$ and Poisson ratio $\nu = 0.3$. Due to the symmetry, an octant of the cylinder is modeled in this case. The displacement obtained from the RPIM is normalized with the analytical solution 1.8248×10^{-5} in [5].

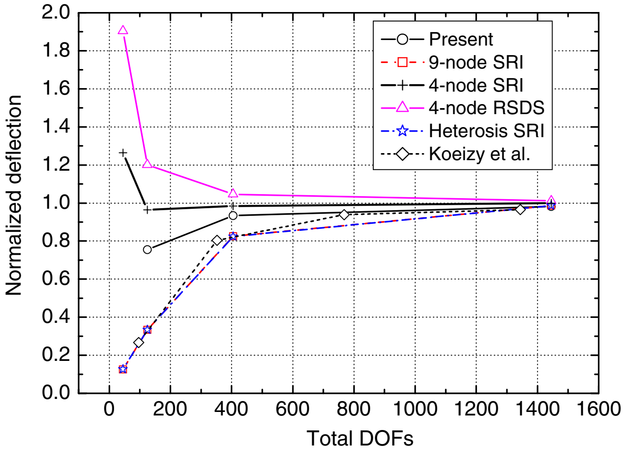

Fig. 5 Comparison of normalized displacements in the Scordelis-Lo roof

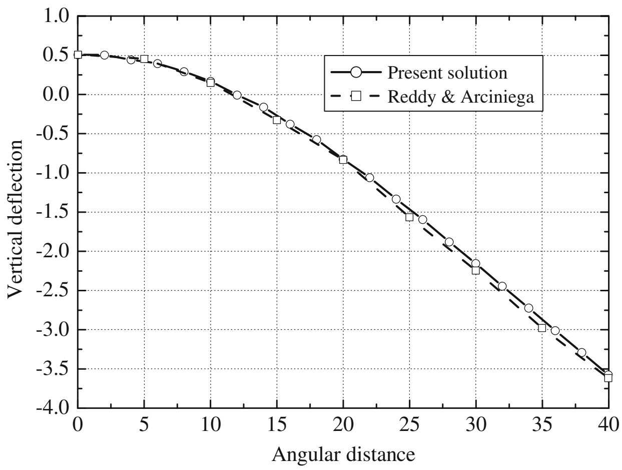

Fig. 6 Vertical deflection of the central line in the Barrel vault

Table 1 Normalized displacement of the Scordelis-Lo roof

	Element	Mesh (nodes)			
		8 × 8 × 1	16 × 16 ×1	32 × 32 ×1	10 × 10 ×2
		(8 × 8)	(16 × 16)	(32 × 32)	
RPIM	Regular	0.906	0.957	1.017	—
	Irregular	1.039	1.190	1.121	
Liu et al. [26]	NUHEX-4	1.016	1.011	1.010	1.045
Liu et al. [27]	NUHEXIN-4	1.162	1.144	1.140	
	HEXDS	1.157	1.137	1.132	

The RPIM solution obtained from a regular nodal distribution, together with FEM results obtained using 4-node, 9-node and Heterosis elements with selective reduced integration, RSDS element [4], and element given by Koziey and Mirza [25], is plotted in Fig. 8. It is seen that the RPIM shows a better convergence performance compared to the FEM when the number of degree of freedom (DOF) exceeds 1300. For DOF less than 1300, the finite elements, excluding

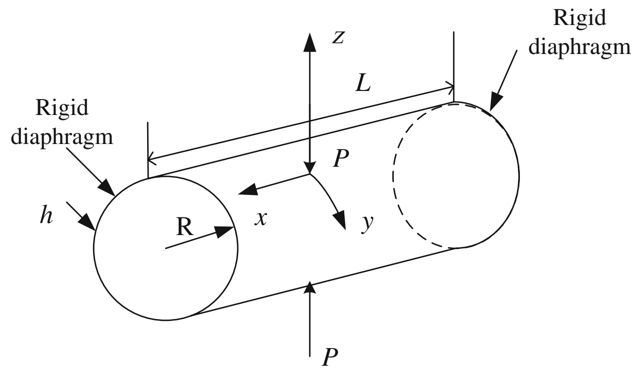

Fig. 7 Geometry of the pinched circular cylinder

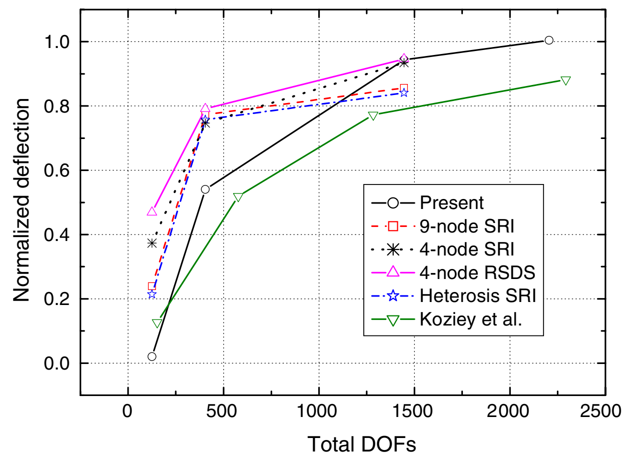

Fig. 8 Comparison of the normalized displacement under point load in the pinched cylindrical shell

the element by Koziey and Mirza [25], demonstrate their superiority in convergent trend over RPIM. Table 2 shows another comparison between the present solution with those attained from NUHEX-4 element and NUHEXIN-4 element [26], and HEXDS element [27]. For the regular nodal distribution, the result derived from the RPIM is as accurate as those from NUHEXIN-4 element [26] and HEXDS element [27] when the number of nodes exceeds 16 × 16. For this case, the RPIM demonstrates a better performance than NUHEX-4 element. For the irregular nodal distribution, the discrepancy is restrained in a range of 6–18.4% when the number of nodes is more than 16 × 16.

5.3 Clamped shallow shell

In this case, the bending deformation is significant in relation to membrane deformation. The shell is clamped at four edges and subjected to a uniform radial pressure distribution $q_0 = 0.04$ psi, as shown in Fig. 9. The geometric parameters are: the length $L = 20$ in, the radius $R = 100$ in, the thickness $h = 0.125$ in, and the span angle $\theta_0 = 0.1$ rad. The material parameters are: Young's modulus $E = 4.5 \times 10^5$

Table 2 Normalized displacement of the pinched cylinder with diaphragms

	Element	Mesh (nodes)		
		$10 \times 10\times$ $2(10 \times 10)$	$16 \times 16\times$ $4(16 \times 16)$	$20 \times 20\times$ $4(20 \times 20)$
RPIM	Regular	0.715	0.943	1.004
	Irregular	0.799	1.062	1.184
Liu et al. [26]	NUHEX-4	0.633	0.870	0.936
Liu et al. [27]	NUHEXIN-4	0.811	0.934	0.980
	HEXDS	0.801	0.945	0.978

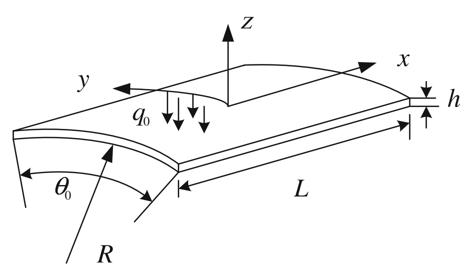

Fig. 9 Clamped cylindrical shell geometry definition

Table 3 Transverse center displacement for clamped cylindrical shell under radial pressure

Present nodes	w(in)	Brebbia and Connor [28]	Palazotto and Dennis [29]	Reddy [30]
11×11	0.01245	0.011	0.01144	0.011349
13×13	0.01197			
15×15	0.01193			
17×17	0.01196			

psi and Poisson ratio $\nu = 0.3$. Only one quarter of the panel is modeled due to the symmetry. This problem has been solved by Brebbia and Connor [28] using Donnell shallow shell strain displacement relations without considering the transverse stresses. Palazotto and Dennis [29] also reported a solution for this problem with transverse stresses included. Due to its high value of length to thickness ratio, the shell is considered to be a thin shell. Hence, the transverse shear deformation is likely to be minimal. The present solution is obtained using a 17×17 regularly distributed nodes. Table 3 shows the present transverse center displacement solution and those given by Brebbia and Connor [25], Palazotto and Dennis [29], and Reddy [30]. A very good agreement is observed.

5.4 Cross-ply cylinder

A simply-supported cross-ply cylinder under internal sinusoidal pressure is considered in this case. The dimensionless material and geometrical properties are: $E_1/E_2 = 25$, $G_{13} = G_{12} = 0.5E_2$, $G_{23} = 0.2E_2$, $\nu_{12} = 0.25$, $L/R = 4$,

Table 4 Central deflection parameters for laminated cylindrical panels under sinusoidal loading

Present laminate	s	$\bar{w}$	Varanda and Bhaskar [31]	Reddy and Arciniega [23]
0°/90°	50	2.2536	2.2420	2.2865
	100	1.3684	1.3670	1.3781
90°/0°/90°	50	0.5468	0.5495	0.5457
	100	0.4726	0.4715	0.4717

Table 5 Maximum deflection of a simply-supported spherical shell panel under central point load

Present laminate	$w \times 10$ (in)	Vlasov [32]	Reddy [30]
Isotropic	0.3947	0.3956	0.3935
Orthotropic	1.2676		1.2644
0°/90°	1.2381		1.2376

$R/h = s$ and $\theta_0 = \pi/8$. The sinusoidal load is expressed as

$$P_s = q_0 \sin\left(\frac{\pi x}{L}\right) \sin\left(\frac{\pi\theta}{\theta_0}\right) \tag{52}$$

where q_0 is a constant. A quarter of the panel is modeled because of the symmetry. Two ratios $s = 50,\ 100$ and two lamination schemes, (0°/90°) and (90°/0°/90°), are considered. A regular nodal distribution of 19×19 is used to achieve the convergent solution. Table 4 shows comparisons of the result from RPIM with the 3D analytical solutions by Varadan [31] and numerical solutions by Reddy [23]. The dimensionless central deflection $\bar{w} = \frac{10E_1}{q_0 R s^3} w$ is introduced in this case. It is seen that RPIM solution agrees well with those in literature.

5.5 Spherical shell panel under point load

A spherical shell panel ($R_1 = R_2 = R$) under point load at the center, as shown in Fig. 10, is studied. The panel is simply supported at all edges. The geometric parameters are: $R_1 = R_2 = R = 96$ in, $a = b = 32$ in, $h = 0.1$ in. Three cases, including an isotropic shell, an orthotropic shell and a shell with a lamination scheme (0°/90°), are considered. For the orthotropic shell and the laminate panel with (0°/90°), the material properties of which have been given in Sect. 5.4. The point load is $P_0 = 100$ lbs. a total of 21×21 nodes are used. Table 5 shows the comparison of present solution with those given by Reddy [30] and Vlasov [32]. Good agreements are observed.

5.6 Spherical shell panel under uniform load

Spherical shell panels with lamination schemes (0°/90°) and (0°/90°/0°) under a uniform load, is studied in this section.

Table 6 Center deflection parameters $\hat{w}$ of spherical shell panels under uniform load $a/h = 100$

Present laminate	R/a	$\hat{w}$	Varanda and Bhaskar [31]	Reddy [30]
0°/90°	5	2.2536	2.2420	2.2865
	10	1.3684	1.3670	1.3781
0°/90°/0°	5	0.5468	0.5495	0.5457
	10	0.4726	0.4715	0.4717

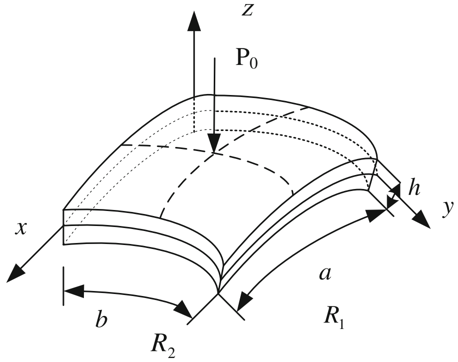

Fig. 10 Simply supported spherical shell panel under central point load

The spherical shell panels have the same material properties as the panel in Sect. 5.5. The number of nodes used in this case is 19 × 19. Table 6 shows the center deflection parameters $\hat{w} = \frac{E_2 h^3}{q_0 a^4} \times 10^3$ for panels with a thickness ratio $a/h = 100$ and radius-to-length ratios $R/a = 5,\ 10$. It is seen that the present solutions agree well with solutions by Reddy [30].

6 Conclusions

A formulation for the shell analysis has been presented using a linearly conforming radial point interpolation method. Both the radial and polynomial basis functions are employed to construct the RPIM shape functions. A strain smoothing technique is introduced for the stabilization of nodal integration. The present formulation is validated by a variety of numerical comparisons. It has been demonstrated that the present method provides very stable and accurate solution for shells under different loading conditions, and effectively eliminates the membrane and shear locking in shells.

References

1. Hughes TJR, Liu WK (1981) Nonlinear finite element analysis of shells: Part I. Three-dimensional shells. Comput Methods Appl Mech Eng 26:331–362
2. Hughes TJR, Liu WK (1981) Nonlinear finite element analysis of shells: Part II. Two-dimensional shells. Comput Methods Appl Mech Eng 27:167–181
3. Belytschko T, Stolarski H (1985) Stress projection for membrane and shear locking in shell elements. Comput Methods Appl Mech Eng 51:221–258
4. Liu WK, Law ES, Lam D, Belytschko T (1986) Resultant-stress degenerated-shell element. Comput Methods Appl Mech Eng 55:259–300
5. Simo JC, Fox DD, Rifai MS (1989) On a stress resultant geometrical exact shell model. Part II: The linear theory. Comput Methods Appl Mech Eng 73:53–92
6. Crisfield M (1986) Finite elements on solution procedure s for structural analysis, I. Linear analysis. Pineridge Press, Swansea
7. Reddy JN, Liu FL (1985) A higher-order shear deformation theory of laminated elastic shells. Int J Eng Sci 23:319–330
8. Krysl P, Belytschko T (1996) Analysis of thin shells by the element-free Galerkin method. Int J Solids Struct 33:3057–3080
9. Noguchi H, Kawashima T, Miyamura T (2000) Element free analyses of shell and spatial structures. Int J Numer Methods Eng 47:1215–1240
10. Li S, Hao W, Liu WK (2000) Numerical simulations of large deformation of thin shell structures using meshfree methods. Comput Mech 25:102–116
11. Liu WK, Han W, Lu H, Li S, Cao J (2004) Reproducing kernel element method. Part I: Theoretical formulation. Comput Methods Appl Mech Eng 193:933–951
12. Li S, Lu H, Han W, Liu WK, Simkins DCJr. (2004) Reproducing kernel element method. Part II: Globally conforming I^m/C^n hierarchies. Comput Methods Appl Mech Eng 193:953–987
13. Simkins DCJr., Li S, Lu H, Liu WK (2004) Reproducing kernel element method. Part IV: Globally compatible $C^n(n \geq$ triangular hierarchy. Comput Methods Appl Mech Eng 193:1013–1034
14. Beissel S, Belytschko T (1996) Nodal integration of the element-free Galerkin method. Comput Methods Appl Mech Eng 139:49–74
15. Bonet J, Kulasegaram S (1999) Correction and stabilization of smoothed particle hydrodynamics methods with applications in metal forming simulations. Int J Numer Methods Eng 47:1189–1214
16. Chen JS, Wu CT, Yoon S, You Y (2001) A stabilized conforming nodal integration for Galerkin mesh-free methods. Int J Numer Methods Eng 50:435–466
17. Wang DD, Chen JS (2004) Locking-free stabilized conforming nodal integration for meshfree Mindlin-Reissner plate formulation. Comput Methods Appl Mech Eng 193:1065–1083
18. Liu GR, Gu YT (2001) A point interpolation method for two-dimensional solids. Int J Numer Methods Eng 0:937–951
19. Wang JG, Liu GR (2002) A point interpolation meshless method based on radial basis functions. Int J Numer Methods Eng 54:1623–1648
20. Liu GR, Dai KY, Lim KM, Gu YT (2003) A radial point interpolation method for simulation of two-dimensional piezoelectric structures. Smart Mater Struct 12:171–180
21. Zhang GY, Liu GR, Wang YY, Huang HT, Zhong ZH, Li GY, Han X (2005) A linearly conforming point interpolation method (LC-PIM) for three-dimensional elasticity problems. Int J Numer Methods Eng (revised)
22. Liu GR, Li Y, Dai KY, Luan MT, Xue W (2006) A linearly conforming RPIM for solids mechanics problems. Int J Comput Methods (in press)
23. Reddy JN, Arciniega RA (2004) Shear deformation plate and shell theories: from Stavsky to present. Mech Adv Mater Struct 11:535–582
24. Reddy JN, Miravete A (1995) Practical analysis of composite laminates. CRC Press, Boca Raton

25. Koziey BL, Mirza FA (1997) Consistent thick shell element. Comput Struct 65:531–549
26. Liu WK, Hu Y, Belytschko T (1994) Multiple quadrature underintegrated finite elements. Int J Numer Methods Eng 37:3263–3289
27. Liu WK, Guo Y, Tang S, Belytschko T (1998) A multiple-quadrature eight-node hexahedral finite element for large deformation elastic analysis. Comput Methods Appl Mech Eng 154:69–132
28. Brebbia, C, Connor J (1969) Geometrically nonlinear finite element analysis. J Eng Mech 463–483
29. Palazotto AN, Dennis ST (1992) Nonlinear analysis of shell structures. AIAA, Washington DC
30. Reddy JN (2004) Mechanics of laminated composite plates and shells: theory and analysis. 2nd edn. CRC press, West Palm Beach
31. Varadan TK, Bhaskar K (1991) Bending of laminated orthotropic cylindrical shells-An elastic approach. Compos Struct 17:141–156
32. Vlasov VZ (1964) General theory of shells and its applications in engineering (translation of Obshchaya teoriya obolocheck I yeye prilozheniya v tekhnike) NASA TT F-99, National Aeronautics and Space Administration, Washington, DC